Biomimetic Ion Channel Regulation for Temperature-Pressure Decoupled Tactile Perception

Naiwei Gao, Jiaoya Huang, Zhiwu Chen, Yegang Liang, Li Zhang, Zhengchun Peng,* and Caofeng Pan*

The perception of temperature and pressure of skin plays a vital role in joint movement, hand grasp, emotional expression, and self-protection of human. Among many biomimetic materials, ionic gels are uniquely suited to simulate the function of skin due to its ionic transport mechanism. However, both the temperature and pressure sensing are heavily dependent on the changes in ionic conductivity, making it impossible to decouple the temperature and pressure signals. Here, a pressure-insensitive and temperature-modulated ion channel is designed by synergistic strategies for gel skeleton's compact packing and ultra-thin structure, mimicking the function of the temperature ion channel in human skin. This ion-confined gel can completely suppress the pressure response of the temperature sensing layer. Furthermore, a temperature-pressure decoupled ionic sensor is fabricated and it is demonstrated that the ionic sensor can sense complex signals of temperature and pressure. This novel and effective approach has great potential to overcome one of the current barriers in developing ionic skin and extending its applications.

1. Introduction

Skin-mimic tactile perception has attracted extensive research attention because of their applications in the upcoming era of intelligence, such as artificial intelligence,[1–4] merge reality,[5–10] telemedicine technologies,[11–13] as well as their potential ability to shield tactile-loss patients (Hansen's disease) from extreme temperature and pressure damage, for example, electronic skin patches and intelligent sensing system.[14–21] However, traditional skin-mimic sensors usually suffer from the problem of the temperature-pressure coupling. This directly leads to the failure of traditional bionic sensors and severely reduces the accuracy of the human body in determining danger signals. Much effort has been dedicated to developing various temperature-pressure decoupled multimode sensors by integrating temperature-responsive units (based on thermos-resistive, pyroelectric, and thermoelectric effects) and pressure sensors (based on piezo-resistive, piezoelectric, and triboelectric effects).[22–34] Flexible all-organic temperature-pressure dual-mode sensors have been designed by integrating polyaniline-based nanocomposites with thermoelectric effects and poly(vinylidene fluoride-*co*-trifluoroethylene) films with piezoelectric effects.[35] Pyramidal pressure sensors without temperature dependence were successfully prepared using a temperature-insensitive alumina dielectric layer.[36] Potentiometric temperature-pressure sensors could also effectively split the temperature-pressure signal.[37] Although these previous works have indicated significant value in temperature and pressure decoupling, there is still a lack of studies on temperature-pressure decoupled ionic sensors, which are represented by widely studied hydrogels and ionic gels.[38–51] Hydrogels and ionic gels are becoming competitive alternatives to mimic human skin, benefiting from their excellent stretchability, high ductility, high transparency, and skin-like ion transport mechanisms.[52–63] Achieving temperature-pressure decoupling for ionic sensors has become one of the critical problems that need to be solved urgently.

The recent discovery of receptors for touch or pressure sensing by David Julius and Ardem Patapoutian, winners of the 2021 Nobel Prize in Physiology or Medicine, has improved our understanding of how the ionic skin perceives temperature and mechanical stimuli.[64] However, it is still a rather difficult challenge for hydrogels and ionic gels to identify the target signal from the temperature-pressure composite signals. The thermosensitive *N*-isopropylacrylamide was introduced into the double-network

N. Gao, Z. Peng
Center for Stretchable Electronics and Nano Sensors
Key Laboratory of Optoelectronic Devices and Systems of Ministry of Education
School of Physics and Optoelectronic Engineering
Shenzhen University
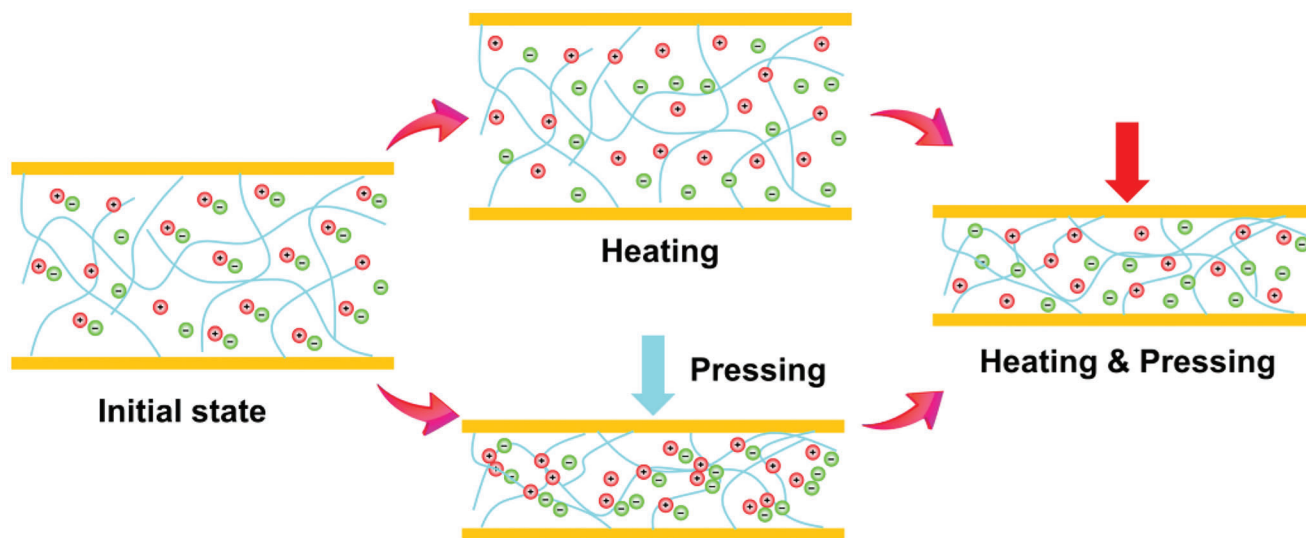Shenzhen 518060, P. R. China
E-mail: zcpeng@szu.edu.cn

J. Huang, Y. Liang, L. Zhang, C. Pan
Beijing Institute of Nanoenergy and Nanosystems
Chinese Academy of Sciences
Beijing 101400, P. R. China
E-mail: cfpan@binn.cas.cn

J. Huang, C. Pan
School of Nanoscience and Technology
University of Chinese Academy of Sciences
Beijing 100049, P. R. China

Z. Chen
Department of Chemistry
Renmin University of China
Beijing 100872, P. R. China

ADVANCED
SCIENCE NEWS
www.advancedsciencenews.com

NANO · MICRO
small
www.small-journal.com

Scheme 1. The temperature and pressure sensing mechanisms of ionic materials. When heating the ionic materials, the anions and cations will be dissociated under the influence of the temperature. When pressing the ionic materials, the micro-conductive channels will be changed the compression of the ionic materials. When applying both temperature and pressure, the change in ionic conductivity is not a simple linear superposition of the response of the two factors.

hydrogels, which are composed by poly(vinyl alcohol-graphite oxide) and poly (acrylic acid-Fe^{3+}), to achieve dual-mode detection for temperature and pressure signals.[65] Temperature-pressure dual-mode response of thermoplastic polyurethane films loaded with ionic liquids was prepared by a simple combination of electrospinning and ultrasonication.[66] A simple heating-cooling photopolymerization method was also developed for the temperature-pressure dual-mode ionic sensors composed of physically cross-linked agarose/ poly (2-hydroxyethyl acrylate) double-network ionic gels.[67] Although these works have provided important explorations of gel-like dual-mode sensors, the issue of signal coupling between the different signals is still not addressed.[68,69] This is mainly because the ionic conductivity is strongly influenced by temperature, and the structure design is difficult to deal with the temperature disturbance caused by the ionic conductivity change.[70–76] In addition, due to the natural viscoelasticity and free ions of ionic gels, the thermoelectric or thermal resistance properties of the ionic material are also easily disturbed by the pressure (**Scheme 1**). Very recent research has demonstrated that ionic relaxation kinetics can effectively differentiate between strain and temperature signals received by ionic sensors.[77] Nevertheless, the coupling of pressure and temperature has still not been well-investigated. Thus, it is still an unsolved problem to design the temperature-pressure decoupled ionic sensors.

2. Ionic Skin and Ion-Confined Gels

Here, we presented for the first time a synergistic strategy of thinning ion-confined gels to inhibit the alteration of the ionic conductive channel of ionic gels, and thus prepare a temperature-pressure decoupled ionic sensor. According to our earlier research, even though both the temperature and pressure responses of ionic sensors are dependent on the response of ionic conductivity to external stimulus, these two sensing processes are significantly different. Specifically, temperature sensors rely largely on the influence of temperature on the dissociation-coupling of anions and cations, whereas pressure sensors rely mostly on alterations in the conductive channel of the ionic material under pressure. Therefore, blocking the change in the conductive channel of the ionic gel will effectively inhibit its pressure response, which allows the temperature and pressure signals to be decoupled. As shown in **Figure 1**a, two ion channel proteins, TRPV1 and Piezo2, play a significant role in the skin's sense of temperature and pressure signals. To mimic the function of the skin, we designed a series of ionic gels that were cross-linked by double-bond-substituted ionic liquids (3-allyl-1-vinyl-1H-imidazolium bromide (IL_3), 3-butenyl-1-vinyl-1H-imidazolium bromide (IL_4), 3-hexenyl-1-vinyl-1H-imidazolium bromide (IL_6)), and acrylates (Methyl Acrylate (MA), Ethyl Acrylate (EA), Butyl Acrylate (BA)). Through the introduction of double bonds, ionic liquids can not only possess the inherent advantages of ionic liquids, such as negligible saturation vapor pressure, high thermal stability, and broad electrochemical window, but are also imparted with good photo-cross-linking properties.[78–82] A further benefit of utilizing ionic liquids as cross-linkers is that ionic liquids are directly attached to the acrylate main chains via the covalent bonds, therefore eliminating the tiny phase gaps which were usually caused by different polarities. This conductive ionic cross-linking agent imparts tunable mechanical and electrical characteristics to the ionic gel, making it an ideal material for the fabrication of temperature-pressure decoupled ionic sensors. Importantly, owing to the covalent bonds between the ionic cross-linker and the
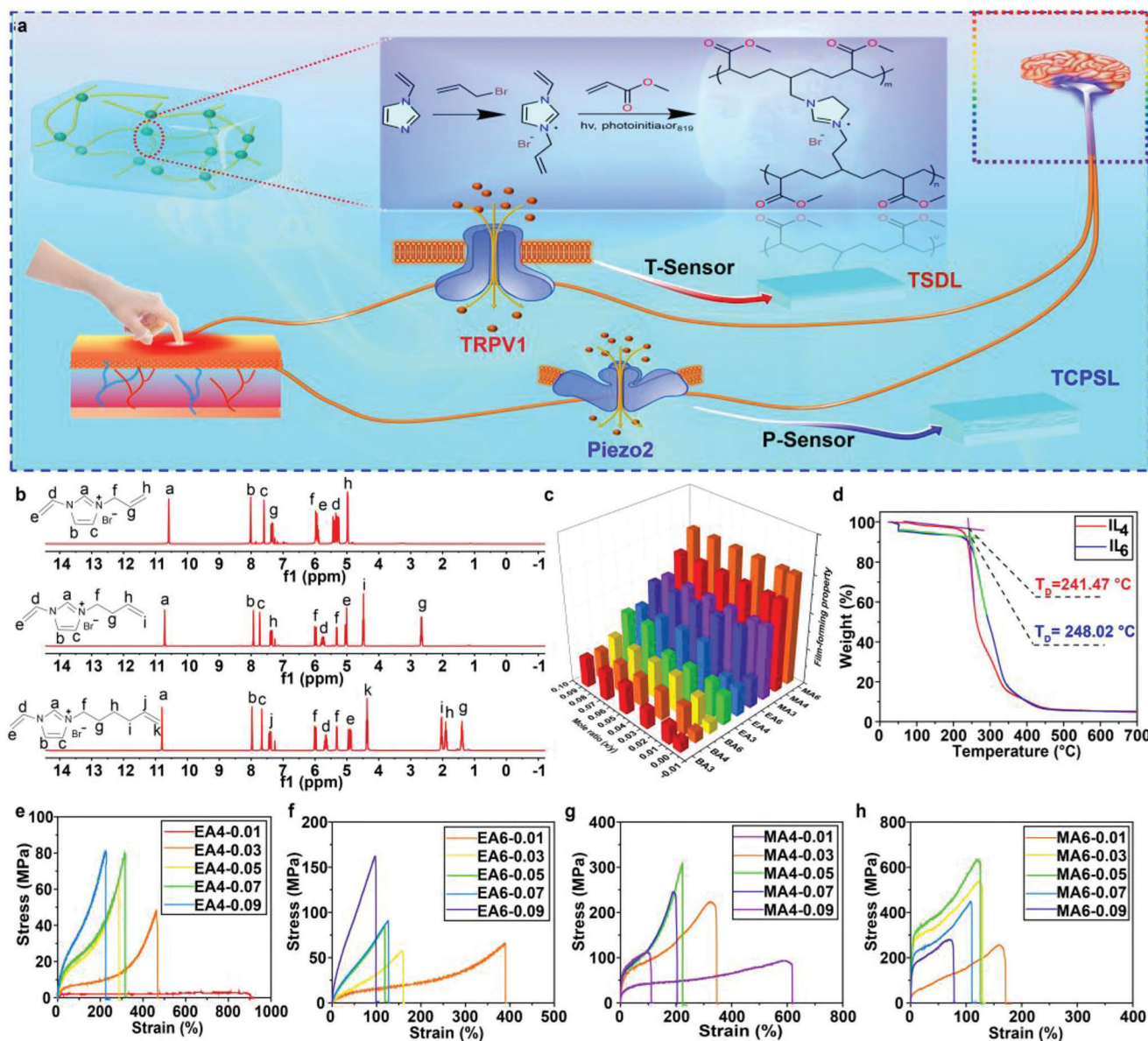
Figure 1. Preparation and characterization of ionic gels. a) Scheme of the structure of ionic gels and the skin-mimic mechanism of the TSDL and the TCPSL. b) ^{1}H NMR spectra of 3-allyl-1-vinyl-1H-imidazolium bromide (IL$_3$), 3-butenyl-1-vinyl-1H-imidazolium bromide (IL$_4$), 3-hexenyl-1-vinyl-1H-imidazolium bromide (IL$_6$). c) Qualitative demonstration of the film-forming properties of different component ionic gels. Above the blue line box indicates good film formation, below indicates poor film formation. d) TGA curves of IL$_4$ and IL$_6$. e–h) Tensile strain tests of ionic gels with different components and molar ratios. The label in the top right corner of the picture shows the detailed components.

acrylate backbone, the ionic conductive channel will not be significantly altered even when pressure is applied; additionally, a thinning strategy is used to further inhibit the alteration of the ionic conductive channel under pressure, resulting in a pressure-insensitive temperature-sensitive decoupling layer (TSDL). The integration of the TSDL with the temperature-corrected pressure sensing layer (TCPSL) that has an outstanding pressure sensitivity may effectively imitate the function of ion channel proteins and decouple the temperature and pressure signals. The exact decoupling process will be discussed in greater depth in a subsequent section.

The chemical structures of the three double-bond-substituted ionic liquids (IL$_3$, IL$_4$, and IL$_6$) are characterized by the ^{1}H NMR spectra in Figure 1b, and the corresponding shift peaks can be assigned. As depicted in Figure 1c, the film-forming properties of the cross-linked ionic gels revealed that the longer the substituent chain of ionic cross-linker is, the better the film-forming property of ionic gels are. The larger the side group of the acrylate main chain is, the worse the film-forming property of ionic gels are. This is mostly owing to the strong link between the film-forming characteristics of the ionic gels and the orderly stacking of macromolecules. Longer substituent chains will stack more closely with

**ADVANCED
SCIENCE NEWS**

www.advancedsciencenews.com

NANO · MICRO

small

www.small-journal.com

the polymer's main chain, which can improve the film-forming characteristic. Otherwise, the increased spatial resistance of the bigger acrylate side groups is harmful to the formation of the film. Taking BA3-0.09 (main chain: BA; cross-linker: IL_3; 0.09: molar ratio of IL_3 to BA) as an example, the ionic gel composed of BA3-0.09 is in a viscous flow state, while the ionic gel MA6-0.09 can form a film with outstanding characteristics. By evaluating the film-forming capabilities of ionic gels, two main chain molecules (EA, MA) and two ionic cross-linkers (IL_4, IL_6) were chosen for the creation of following ionic sensors. Thermogravimetric analysis (TGA) tests showed the strong thermal stability of the ionic cross-linkers (Figure 1d), with the thermal breakdown temperatures of IL_4 and IL_6 being 241.47 and 248.02 °C, respectively. This is crucial for the applications of the ionic temperature sensors. Stress-strain tests further confirmed that the ionic gels comprised of long-chain-substituted ionic cross-linkers and small acrylate side groups exhibit higher modulus (Figure 1e–h). In addition, it can be concluded that the modulus of the ionic gel increases with the amount of the ionic cross-linker.

3. Pressure-Insensitive Temperature Sensing Decoupling Layer

As previously stated, the key to fabricate the pressure-insensitive ionic temperature sensors are to prevent the change of the ionic conductive channel under pressure. As shown in **Figure 2**a, covalent and ionic bonds bind the anions and cations of ionic liquids to the molecular chains of the ionic gels. When the pressure is applied, the ionic distribution inside the ionic gels stays mostly fixed, preventing the free movement of ionic components and restricting the ionic gels' pressure response. Besides, coupled with the technique of thinning the ionic gels, the deformation of the thinned ionic gels under pressure is reduced to further minimize the pressure response of the ionic gels. To facilitate the test, a Peltier device was used as the heat source for the subsequent temperature test. And we used an infrared camera to obtain the relationship between voltage and temperature of the Peltier device for establishing the link between the sensor response and temperature directly (Figure S1, Supporting Information). Figure 2b–e illustrate the temperature responses of the ionic gels with different components. It can be observed that the temperature responsiveness of the ionic gels deteriorates with increasing cross-linking ratio. It is additionally noted that there is no association between the temperature response of the ionic gels and the components of ionic gels, which is mostly attributed to the calculation method of the relative conductivity. Despite this, the comparison of the absolute conductivity of the temperature response reveals a clearer pattern (Figure 2f–i). To improve the temperature responsiveness of the ionic gels, the length of the ionic cross-linker substituent must be shortened while the volume of the side groups of acrylates must be raised. Only then will the molecular chains of the ionic gels have sufficient space for ionic migration when the temperature is altered. The results prove that the ionic gel EA4 have the best temperature responsiveness. In Figure 2j, the thickness of the ionic gel EA4 was lowered to 40 μm, and the pressure response of the ionic gels with different cross-linking ratios was evaluated at various temperatures. A considerable temperature response could be observed when the ionic gel was put on a heated platform at 26.53 °C for 2 min, however, no significant pressure signals were obtained. This demonstrated that the thinned ionic gels successfully prevented the change of the ionic conductivity channel from pressure signal. In addition, the relationship between the pressure insensitivity and the thickness dependency was also investigated (Figure S2, Supporting Information). Only when the thickness of the ionic gel was extended to 320 μm did the ionic gel exhibit a considerable degree of pressure responsiveness at high temperatures. This is primarily attributed to the chemical covalent bonding of the ionic components to the molecular chains. The physical-confined effect of molecular chains on the ionic components plays a significant role in preventing the change of the ionic conductive channel. The physical-confined function of the molecular chain can be verified by the strain-stress test of the ionic gels (Figure S3, Supporting Information). There is almost no linear interval in the strain–stress curves, proving that viscosity dominates the viscoelasticity of ionic gels. This viscosity theoretically derives from the physical entanglement of the molecular chains, making the ionic conductive channel in the ionic gels almost unchangeable.

To quantify the pressure-insensitive performance of the ion gel, we define the ratio of the pressure-responsive conductivity change ($\Delta G_P / \Delta G_0$) to the total conductivity change ($\Delta G_{T\&P} / \Delta G_0$) as the pressure decoupled coefficient β_P. Similarly, we define the ratio of the temperature-responsive conductivity change ($\Delta G_T / \Delta G_0$) to the total conductivity change ($\Delta G_{T\&P} / \Delta G_0$) as the temperature decoupled coefficient β_T. The mathematical expressions of the β_P and β_T are shown as the following.

$$\beta_P = \frac{\Delta G_P / \Delta G_0}{\Delta G_{T\&P} / \Delta G_0} = \frac{\Delta G_P}{\Delta G_{T\&P}} \tag{1}$$

$$\beta_T = \frac{\Delta G_T / \Delta G_0}{\Delta G_{T\&P} / \Delta G_0} = \frac{\Delta G_T}{\Delta G_{T\&P}} \tag{2}$$

According to the Equations (1) and (2), the sum of the pressure decoupled coefficient β_P and the temperature decoupled coefficient β_T is 0. When the input signal is a temperature-pressure composite signal, if $\beta_P = 1$, the pressure response of the ion sensor is temperature-insensitive; if $\beta_T = 1$, the temperature response of the ion sensor is pressure-insensitive; if β_P and β_T are in between 0 and 1, the temperature response and the pressure response of the sensor are coupled. According to Figure 2k, the β_T of the ionic gels at different temperatures can all reach above 0.99, which further confirms that the temperature response of the ion gels is pressure insensitive.

4. Temperature-Corrected Pressure Sensing Layer

Unlike the design of temperature sensors, ionic pressure sensors (also called TCPSL), which are another key structure in temperature-pressure decoupled ionic sensors, need to cause a relatively significant change in the ionic conductive channel under the pressure. Since the ionic gels described above are lack of elasticity, polyethylene glycol-400 (PEG-400) was added to the ionic gels, which can swell the ionic gels. This will be helpful to increasing their pressure sensitivity (Figure S4, Supporting Information). **Figure 3**a depicts the sensing mechanism of the TCPSL. After the PEG-400 is introduced, the ionic component
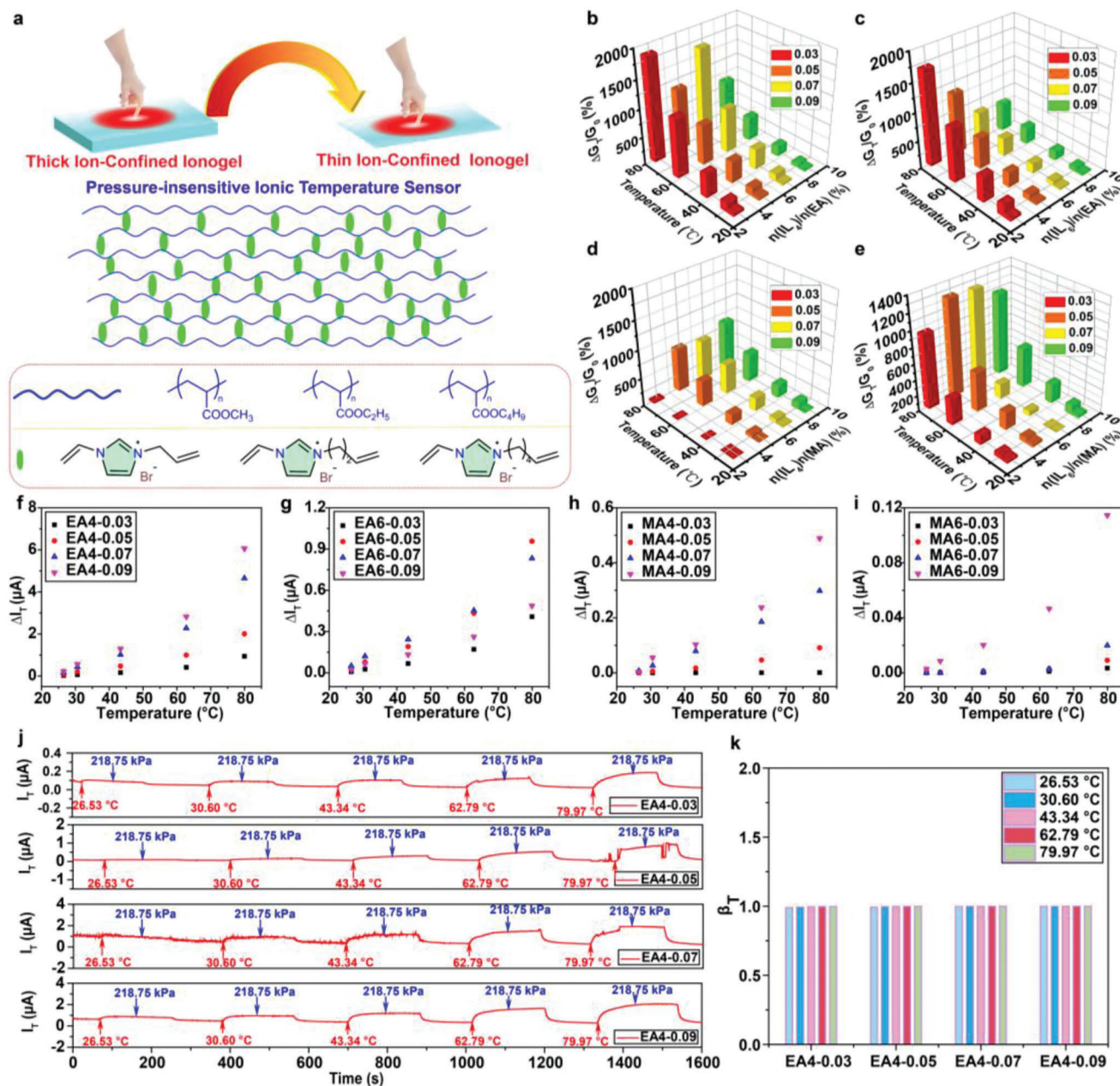
Figure 2. Sensing mechanisms and performance testing of TSDL. a) Illustration of the strategy of thinning ion-confined ionic gels. b–e) 3D histogram of the relative conductivity response to temperature for ionic gels with different components. f–i) The absolute current change against temperature for ionic gels with different components. j) Pressure-insensitive tests of the temperature response of ionic gels (EA4-0.03, EA4-0.05, EA4-0.07, EA4-0.09) after thinning. k) The histograms of the temperature decoupling coefficients of the samples in (j).

of the ionic gels will be dissolved in PEG-400. As there is a certain polarity difference between the ionic gels and PEG-400, the PEG-400 exists in the ionic gels in the form of micro-droplets. When the pressure is applied, the droplets fuse each other to generate a more conductive channel, making the ionic gels more pressure-sensitivity. The changes in the relative conductivity of the different component ionic gels under pressure are shown in Figure 3b–e. In general, the pressure responsiveness of the ionic gels increases as its cross-linking degree decreases. However, absolute conductivity change is also essential for the pressure sen-

sors. In theory, the higher the fluctuation in absolute conductivity is, the fewer requirements a sensor has for post-amplification circuits is. It can be used to simplify the design process of the device. As seen in Figure 3f–i, the absolute conductivity change of the pressure response increases with increasing the degree of cross-linking. In addition, when the degree of cross-linking increases, the ionic gels become more elastic, and their response times decrease gradually (Figure S5, Supporting Information). When the ionic gel is MA6-0.09-0.3 (main chain: MA; cross-linker: IL_6; 0.09: molar ratio of IL_6 to MA; 0.3: molar ratio of PEG-400 to MA),
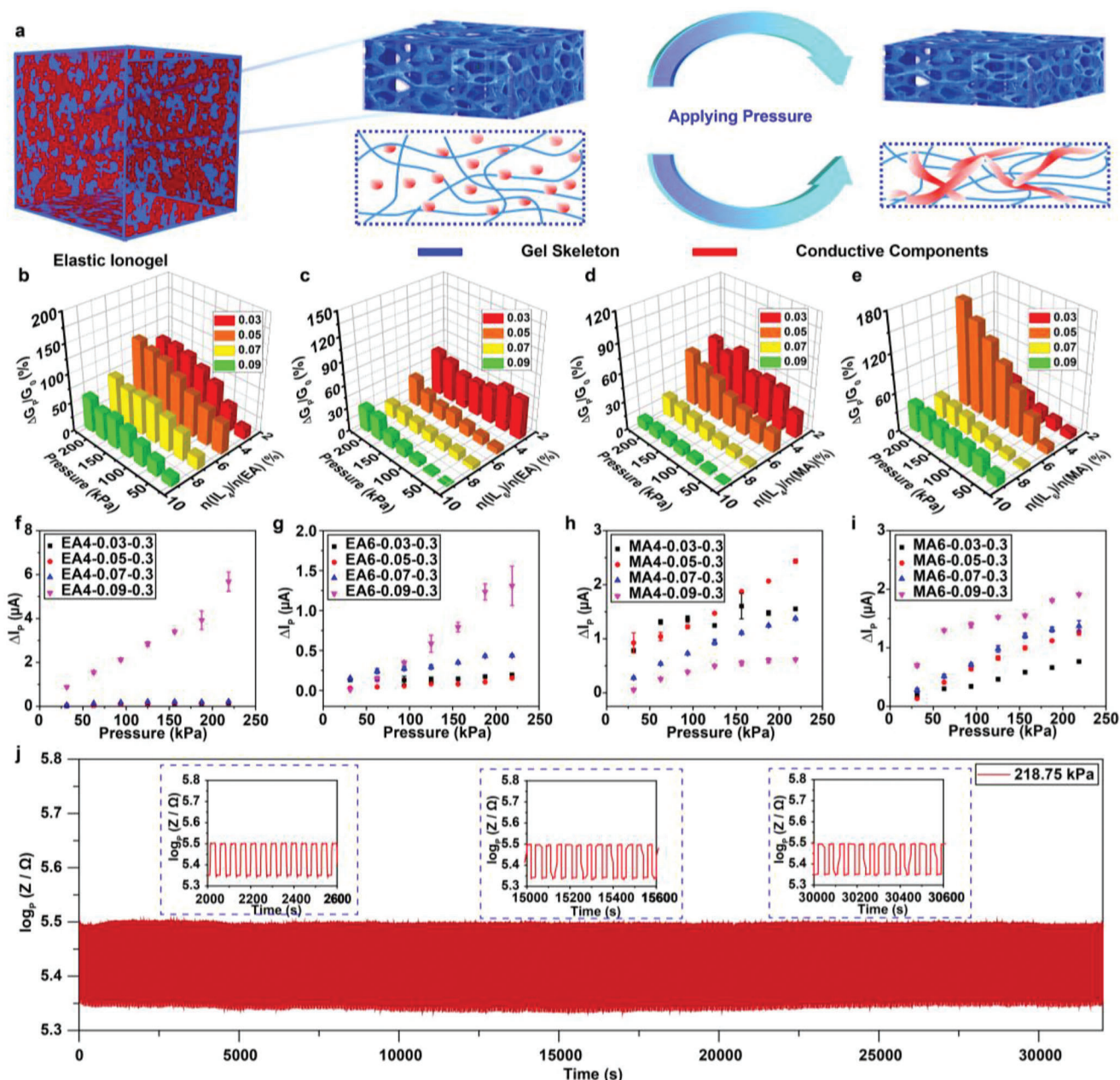
Figure 3. Sensing mechanisms and performance testing of TCPSL. a) Illustration of the ionic pressure sensors. b–e) 3D histogram of the relative conductivity response to pressure for ionic gels with different components. f–i) The absolute current change against pressure for ionic gels with different components. j) Cyclic stability testing of pressure sensors (MA6-0.09-0.3).

the pressure response time can be lowered to 0.22 s. Therefore, the subsequent design of the TCPSL will utilize the ionic gel under this component. The compressive stress-strain cycle curves of ionic gels also confirm this (Figure S6, Supporting Information). The stress–strain curve of the ionic gel MA6-0.09-0.3 has essentially no hysteresis behavior. The TCPSL based on this ionic gel has also shown extremely good pressure cycling stability, retaining a very stable response throughout 2000 pressure tests of 218.75 kPa (Figure 3j).

5. Temperature-Pressure Decoupled Ionic Sensor

Based on the above-described pressure sensors (TCPSL) and pressure-insensitive temperature sensors (TSDL), the structure depicted in **Figure 4**a can be used to fabricate temperature-pressure decoupled ionic sensor. Both the TSDL and the TCPSL have a vertically crossed top-bottom electrode arrangement separated by an isolating PET layer to prevent signal interference. When the TSDL is placed as shown in Figure S7, Supporting
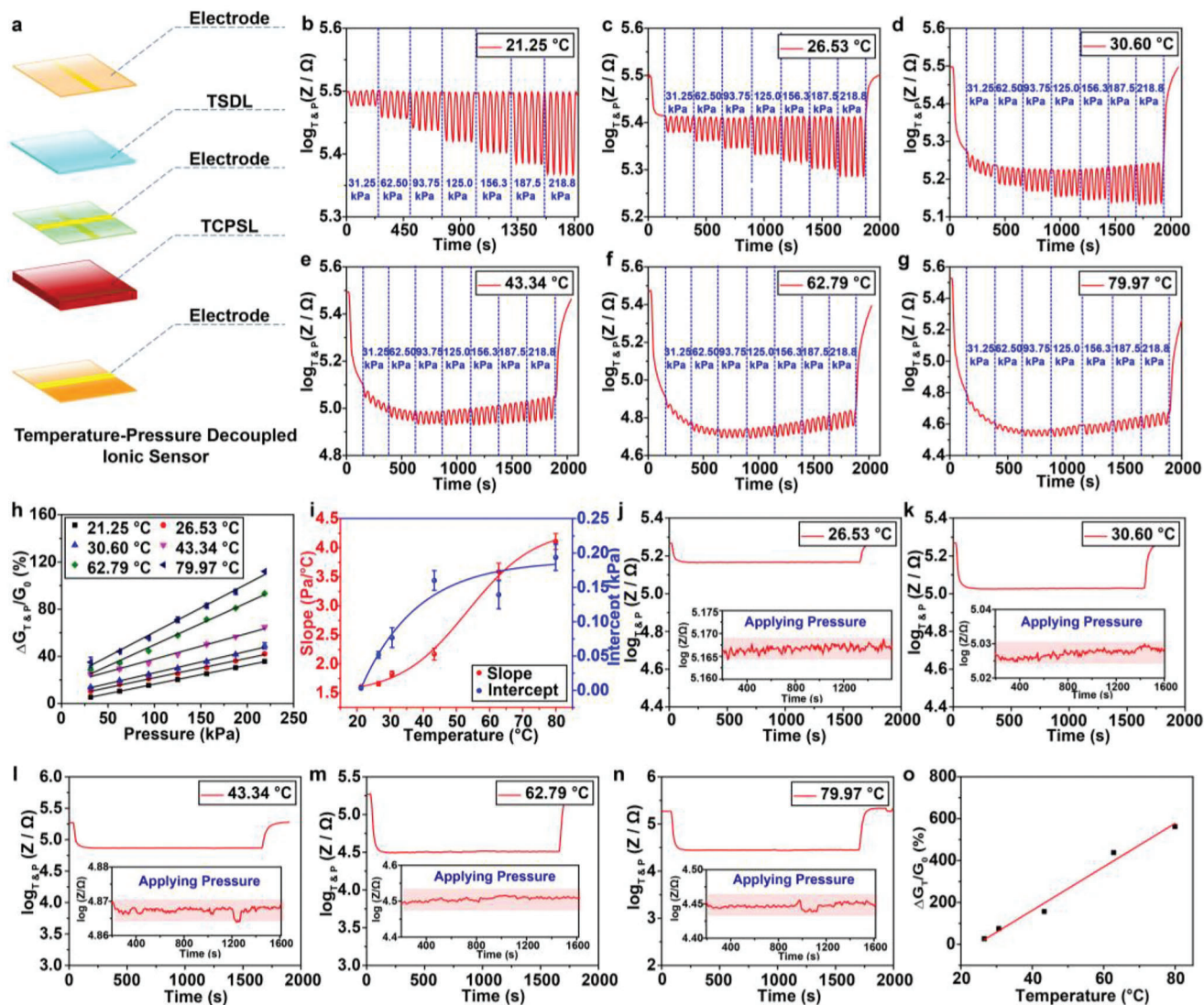
Figure 4. The structure and performance testing of the temperature-pressure decoupled ionic sensor. a) The structure of the temperature-pressure decoupled ionic sensor. b–g) Resistance changes of the TCPSL under different pressures (31.25 kPa, 62.50 kPa, 93.75 kPa, 125.00 kPa, 156.25 kPa, 187.50 kPa, 218.75 kPa) at b) 21.25 °C, c) 26.53 °C, d) 30.60 °C, e) 43.34 °C, f) 62.79 °C, g) 79.97 °C. h) Linearity of the relative conductivity changes of the TCPSL against pressure at different temperatures. i) The slope and intercept of the linear relationship in (h) as a function of temperature. j–n) The resistance changes of the TSDL under different pressures (31.25 kPa, 62.50 kPa, 93.75 kPa, 125.00 kPa, 156.25 kPa, 187.50 kPa, 218.75 kPa) at j) 26.53 °C, k) 30.60 °C, l) 43.34 °C, m) 62.79 °C, n) 79.97 °C. o) The response curve of the relative conductivity changes of the TSDL at different temperatures.

Information, it is difficult for the peripheral TSDL to accurately sense the temperature of the central heat source. So here we chose this vertical device configuration. At the initial temperature (21.25 °C), the TCPSL demonstrated an excellent pressure response (Figure 4b). Increasing the temperature to 26.53 °C and simultaneously applying pressure signals to the temperature-pressure decoupled ionic sensor, the TCPSL still exhibited a reasonable pressure response (Figure 4c). But the absolute change of the response decreased gradually when increasing the temperature (Figure 4d–g). We believe that this is mostly because the raising temperature alters the interfacial characteristics of PEG-400 and ionic gels, resulting in a degree fusion of PEG-400. This lowers the space for the pressure-modifiable ionic conductive channel, and thus reducing the absolute pressure response.

Figure 4h provides a summary of the pressure response curves of the TCPSL at various temperatures. Although the absolute response of the TCPSL follows the laws described above, its relative response grows gradually with rising temperature, and the link between pressure and relative conductivity is linear at all temperatures. Figure 4i depicts the slope and intercept of this linear relationship against temperature, respectively. This association can be represented by the Equations (3) and (4).

$$k_p = 1.49 \times 10^{-3} + \frac{2.84 \times 10^{-3}}{1 + 10^{4.25 \times 10^{-2}(53.41-T)}} \tag{3}$$

$$\gamma_p = 0.19 - 0.65 \cdot e^{-T/16.91} \tag{4}$$

where k_p and γ_p are the slope and intercept of this linear relationship, respectively. p represents the pressure. T (°C) is the temperature applied to the temperature-pressure decoupled ionic sensor. Based on these relationships, we can obtain the Equation (5) for the response of the TCPSL,

$$\frac{\Delta G}{G_0} \text{ (TCPSL, \%)} = \left[1.49 \times 10^{-3} + \frac{2.84 \times 10^{-3}}{1 + 10^{4.25 \times 10^{-2}(53.41 - T)}}\right] + \left[0.19 - 0.65 \cdot e^{-T/16.91}\right] \cdot P \quad (5)$$

where $\Delta G/G_0$ (TCPSL, %) is the relative conductivity change of the TCPSL. P (kPa) is the pressure applied to the temperature-pressure decoupled ionic sensor. Since the TSDL is not pressure sensitive, the temperature T may be monitored through the TSDL without the interference of pressure signal (Figure 4j–n). In Figure 4o, the following Equation (6) describes the temperature response curve of the TSDL,

$$\frac{\Delta G}{G_0} \text{ (TSDL, \%)} = -2.53 + 0.10T \quad (6)$$

where $\Delta G/G_0$ (TSDL, %) is the relative conductivity change of the TSDL. Here, the temperature T can be calculated by Equation (6). Then we can input the temperature T into the Equation (5) to obtain the pressure P. Finally, the temperature T and pressure P can be decoupled from these two decoupled equations. In addition, the stability of the temperature-pressure decoupled ionic sensor and the sample reproducibility can be better ensured (Figures S8,S9, Supporting Information). According to Tables S1–S4, Supporting Information, the TCPSL of the temperature-pressure decoupled ionic sensor can reach a maximum β_P of 0.59, while the β_T of the TSDL can both reach 0.97, further supporting the key of the decoupling mechanism is pressure-insensitive TSDL (Equation (6)). The function of the TCPSL is to establish the mathematical model with a temperature modification factor under different temperature-pressure composite signals (Equation (5)).

6. Array Test and Robotic Arm Test

To further mimic the functionality of the skin, a sensor array based on a temperature-pressure decoupled ionic sensor was assembled. 10 × 10 temperature-pressure decoupled ionic sensor arrays were prepared as shown in **Figure 5**a. First, the arrayed silver electrodes are processed horizontally on the PET substrate, then ionic prepolymer (without PEG-400) is added dropwise to the VHB tape template covering the arrayed silver electrodes, and after photopolymerization the template is removed to obtain the arrayed temperature sensing layer, on which the arrayed silver electrodes are processed vertically to produce the arrayed temperature sensing layer. The PET substrate is then flipped over, and the arranged pressure sensing layer (dropwise addition of ionic prepolymer containing PEG-400) is produced on the reverse side of the PET according to the same craft. Figure 5b illustrates the arrayed display of a temperature-pressure decoupled ionic sensor array under the "T" model's patterned pressure. Similarly, "E" and "H"-shaped models are also utilized to measure the temperature-pressure decoupled ionic sensor array and validate the correctness of this design (Figure 5c,d). For the relatively simple model, the imaging quality of the sensor array is improved

more obviously (Figure 5e). The thermal imaging performance of the sensor array is tested by releasing the pressure and supplying power to the thermoelectric device to raise the temperature of the thermoelectric device (Figure 5f). Due to the presence of thermal field, there is a certain thermal field diffusion around the thermal imaging point, which reduces the thermal imaging quality. At this point, we further apply pressure to the warmed up thermoelectric device, and the imaging quality of the sensor array can be significantly improved by the composite signal of temperature as well as pressure (Figure 5g). As illustrated in Figure 5h, a robotic arm integrated with a temperature-pressure decoupled ionic sensor has been created to simulate skin functions. The robot arm is used to grip objects with different temperatures (Blue cube: 25 °C; Red cube: 70 °C). When the arm grasps a chilly item, it can do so normally since the thing is cold. This initially validates the potential advantages of this ionic sensor. However, when the arm grasps a hot object, the arm's temperature sensor will sound an alert, causing the arm to release its grip on the hot object.

To test the temperature-pressure decoupling performance of our ionic sensors, we tested the decoupled performance of the sensor by pressing a thermal platform with different temperature and pressure against a temperature-pressure decoupled ion sensor. The results are shown in Figure 5i,j. Substituting the data into Equations (5) and (6), we can obtain the theoretical values of the temperature and pressure signals subjected to the sensor at different stages (Figure 5k). The theoretical temperature and pressure values subjected to the six test stages are I: 27.88 °C and 2.56 kPa; II: 27.82 °C and 27.62 kPa; III: 27.96 °C and 57.38 kPa; IV: 39.95 °C and 40.81 kPa; V: 40.16 °C and 175.49 kPa; VI: 40.32 °C and 264.85 kPa). This is very consistent with the practical value of the input signals (I: 27.71 °C and 2.50 kPa; II: 27.71 °C and 25.00 kPa; III: 27.71 °C and 56.25 kPa; IV: 40.03 °C and 43.75 kPa; V: 40.03 °C and 181.25 kPa; VI: 40.03 °C and 268.75 kPa). To further verify the temperature-pressure decoupling performance, we attached the sensor to a human finger and gripped the finger on objects. As shown in Figure 5l, when we grasp the hot object by hand, the response curve of the sensor shows a three-stage process for both the TCPSL and the TSDL. The first stage is when our hand is close to the high temperature object, the resistance of the TCPSL and the TSDL starts to show a slow decrease. This is mainly caused by the temperature field created by the high-temperature object in its periphery. This stage can be used as an early warning stage for arm grip. We can judge the temperature of the object based on the magnitude of the drop in resistance to avoid skin burns caused by high temperatures. The second stage is that our hand has grasped the hot object. The resistance of the TCPSL and the TSDL drops sharply in this stage. The drop in the resistance of the TCPSL includes the change caused by both the high temperature and the pressure of grasping. The drop in the resistance of the TSDL is entirely attributed to the drop caused by the high temperature. This process is the key stage in which we perform signal decoupling. The third stage is the recovery process of the device resistance when we slowly remove the object. We substitute the temperature as well as the pressure signal measured by the sensor into our decoupling model to obtain the temperature of the object and the force of the grip. The relevant data are shown in Figure 5m. This further confirms the advantages and potential applications
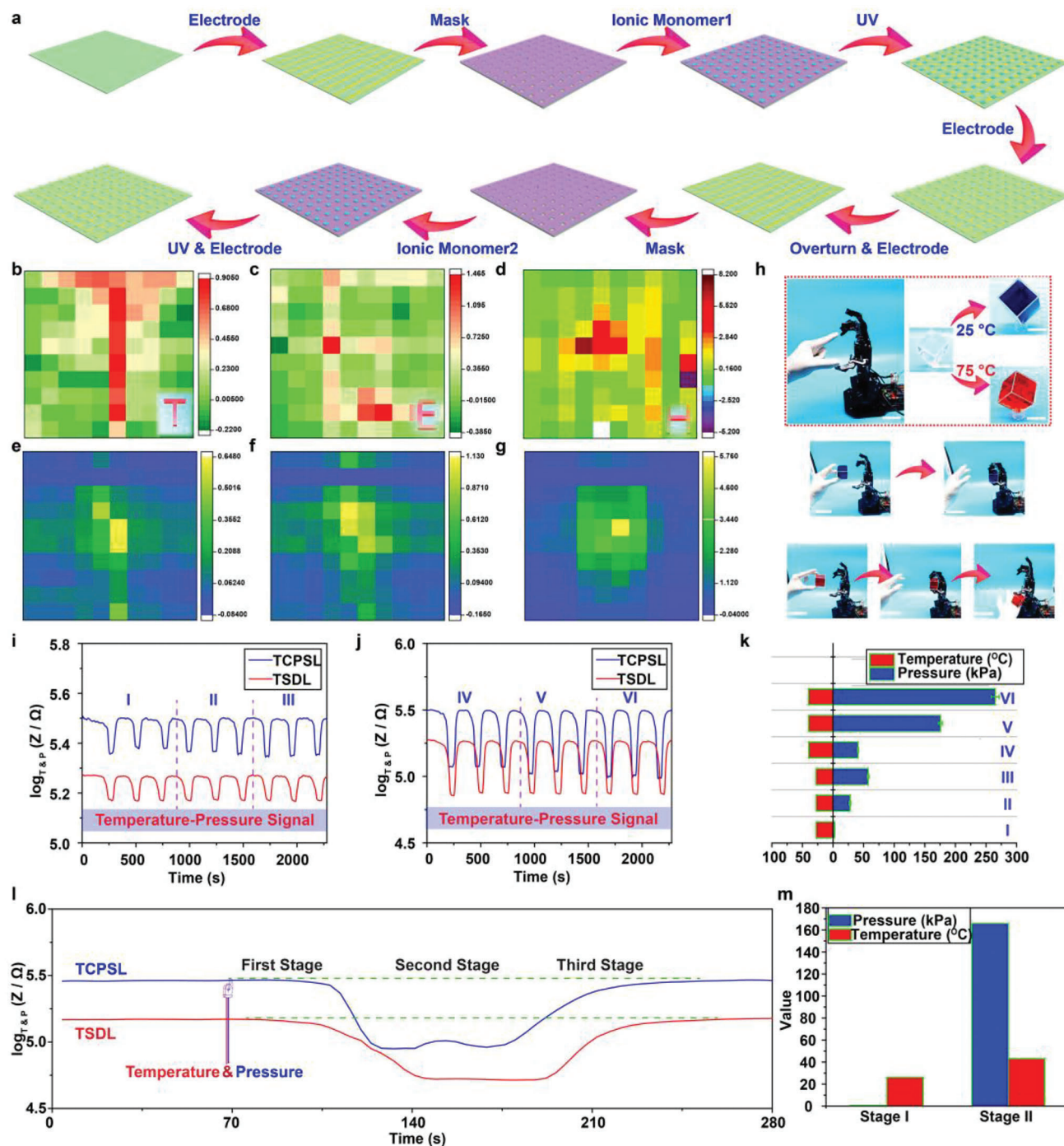
Figure 5. Array test and arm test of temperature-pressure decoupled ionic sensor. a) The preparation process of the temperature-pressure decoupled ionic sensor arrays. Arrayed display of sensor arrays under patterned pressure (3.5 N) at room temperature. The corresponding patterning pressures are b) T, c) E, d) H, respectively. e) Square-mold arrayed display of sensor arrays under the pressure of 3.5 N without heating. f) Square-mold arrayed display of sensor arrays under a high temperature of 50 °C without pressure. g) Square-mold arrayed display of sensor arrays under the a high temperature of 50 °C and the pressure of 3.5 N. h) The above image is the robotic arm with an integrated temperature-pressure decoupled ionic sensor (Blue cube: 25 °C; Red cube: 70 °C). The middle image is the reaction process of the robot arm after grasping the blue cube. The bottom image is the reaction process of the robot arm after grasping the red cube. i) Sensor response under combined temperature and pressure signals (I: 27.71 °C and 2.50 kPa; II: 27.71 °C and 25.00 kPa; III: 27.71 °C and 56.25 kPa). j) Sensor response under combined temperature and pressure signals (IV: 40.03 °C and 43.75 kPa; V: 40.03 °C and 181.25 kPa; VI: 40.03 °C and 268.75 kPa). k) Histogram of the temperature as well as pressure signals solved from the decoupled equation. l) The temperature-pressure decoupling test curves of the temperature-pressure decoupled ionic sensors during gripping high temperature process. m) Temperature-pressure histogram after decoupling.

**ADVANCED
SCIENCE NEWS**

www.advancedsciencenews.com

**NANO · MICRO
small**

www.small-journal.com

of our temperature-pressure decoupled sensor in the field of ionic skin.

7. Conclusion

In summary, to address the issue of temperature-pressure coupling in the ionic sensors, we devised ionic gels with pressure-insensitive characteristics. Furthermore, we presented a novel strategy for controlling the ionic conductivity of the gels by simply thinning the gels. When the ionic gel is thinned to 40 μm, the change in the ionic conductivity can be totally blocked, successfully suppressing the pressure response of the ionic gel. This material is suitable for the fabrication of pressure-insensitive ionic temperature sensors. On another hand, we employed PEG-400 as a solvent for the same ionic gel to create a pressure-sensitive material. Notably, the response mechanism of the prepared pressure sensing material is identical to that of a normal ionic gel, sensitive to both temperature and pressure. Only by merging it with the pressure-insensitive ionic gel layer is it possible to separate the temperature and pressure signals. The temperature-pressure decoupled ionic sensor developed here effectively resolves one of the most challenging issues in the field of ionic skins and will significantly increase the application potential of ionic sensors in the field of haptics.

8. Experimental Section

Materials: Methyl acrylate (AR), ethyl acrylate (AR), butyl acrylate (AR), and 1-vinylimidazole (AR) were purchased from Aladdin Industrial Corporation. Allyl bromide, 4-bromo-1-butene and 6-bromo-1-hexene were bought from Beijing InnoChem Science & Technology Co., Ltd. Ethyl alcohol (AR) and PEG-400 (AR) were bought from Alfa Aesar. The UV-curing lamp (60 W), polytetrafluoroethylene (PTFE) molds, conductive silver pastes, and robotic arms were all obtained from Taobao.com. Peltier devices (TEC1-12705) and other basic electronic components were purchased from Zhongfa electronic Building.

Characterizations: ^{1}H-NMR spectra were recorded on a Bruker spectrometer operating at 400 MHz. A thermal-gravimetric analysis (TGA) was operated by a Q50 TGA (TA Instruments). The strain–stress tests were conducted using tensile machine (Yuelian YL-S71) at a speed of 10 mm min^{-1}. All the heat sources required for temperature sensing were implemented through the Peltier device, which can control the temperature by adjusting its voltage input. The temperature change was recorded by the Fluke infrared camera (Tix 640). Every temperature cycle consisted of two processes: heating (2 min) and cooling (2 min). The pressure tests were provided by Digital manometers (Mark-10) to meet the requirements of pressure sensing. Simultaneous temperature and pressure signal testing was achieved by combining Peltier device and digital manometers. The electronic measurements were conducted on a CHI660E electrochemical workstation with a fixed voltage of 1.0 V. The electrical characterization platform interfaced with the sensor array through a customized 96-pin probe card installed on the probe station. All the pixels were individually addressable by using the multichannel current testing system (Keithley 2612). The V–t curves from 10 pixels in a typical single-channel line scan were obtained through a multichannel voltage testing system (NI PXI-2530).

Synthesis of Double-Bond-Substituted Ionic Liquids: Allyl bromide (0.5 mol) and 1-vinylimidazole (0.5 mol) were added dropwise to a round bottom flask, followed by dropping acetonitrile (5.0 mL). The reaction was carried out at 80 °C for 24 h with reflux. At the end of the reaction, the solvent and the unreacted substrate were removed by spin evaporation. Then a brownish ionic liquid 3-allyl-1-vinyl-1H-imidazolium bromide (IL$_3$) could

be obtained. Yield: 90.2%. ^{1}H-NMR (400 MHz, IL$_3$, CDCl$_3$, δ): 10.58 (t, J = 3.98 Hz, 1 H), 8.01 (t, J = 3.96 Hz, 1 H), 7.60 (t, J = 3.97 Hz, 1 H), 7.36 (dd, J = 24.48 Hz, 1 H), 5.43 (d, J = 34.04 Hz, 2 H), 5.32 (t, J = 36.80 Hz, 1 H), 5.32 (d, J = 6.89 Hz, 2 H).The other two ionic liquids 3-butenyl-1-vinyl-1H-imidazolium bromide (IL$_4$) and 3-hexenyl-1-vinyl-1H-imidazolium bromide (IL$_6$) could be synthesized by the same process, simply by replacing allyl bromide (0.5 mol) with 4-bromo-1-butene (0.5 mol) and 6-bromo-1-hexene (0.5 mol) respectively. Yield (IL$_4$): 91.4%. ^{1}H-NMR (400 MHz, IL$_4$, CDCl$_3$, δ): 10.07 (t, J = 3.06 Hz, 1 H), 7.94 (t, J = 3.05 Hz, 1 H), 7.74 (t, J = 3.06 Hz, 1 H), 7.37 (dd, J = 24.52 Hz, 1 H), 6.01 (d, J = 18.15 Hz, 1 H), 5.77 (t, J = 40.48 Hz, 1 H), 5.32 (d, J = 11.71 Hz, 1 H), 5.01 (d, J = 27.34 Hz, 2 H), 4.48 (d, J = 17.30 Hz, 2 H), 2.65 (d, J = 21.45 Hz, 2 H). Yield (IL$_6$): 92.1%. ^{1}H-NMR (400 MHz, IL$_4$, CDCl$_3$, δ): 10.80 (t, J = 2.85 Hz, 1 H), 7.97 (t, J = 2.85 Hz, 1 H), 7.67 (t, J = 2.85 Hz, 1 H), 7.40 (dd, J = 24.45 Hz, 1 H), 6.01 (d, J = 18.88 Hz, 1 H), 5.67 (t, J = 41.48 Hz, 1 H), 5.32 (d, J = 12.11 Hz, 1 H), 4.92 (d, J = 33.36 Hz, 2 H), 4.37 (d, J = 14.93 Hz, 2 H), 2.03 (q, J = 21.62 Hz, 2 H), 1.88 (dd, J = 28.62 Hz, 2 H), 1,41 (dd, J = 29.58 Hz, 2 H).

Preparation of Viscous Ionic Gels with Different Components: According to the synthetic process in Figure 1a, three different ionic cross-linkers (IL$_3$, IL$_4$, IL$_6$) and three different main chain molecules (MA, EA, BA) were used to fabricate a series of ionic gels by adjusting their molar ratios. Here, the photoinitiator 819 was added to the monomers with certain molar ratios. Then they were put into the PTFE mold (Length: 4.0 cm; Width: 1.0 cm; Height: 0.3 cm). After 20 min of photopolymerization, the corresponding ionic gel could be obtained. After extensive experimental exploration, IL$_4$, IL$_6$, MA, and EA were selected as monomers. Also, the molar ratios of 0.01, 0.03, 0.05, 0.07, and 0.09 were selected to prepare the ionic gels that were used for the strain–stress tests.

Preparation of Elastic Ionic Gels with Different Components: Using the ionic gels obtained above, the PEG-400 was added to the monomers in a molar ratio of 0.3 (n(PEG-400) : n(MA or EA)). Similarly, the molar ratios of 0.03, 0.05, 0.07, and 0.09 were selected to prepare the elastic ionic gels that were used for the strain–stress tests.

Fabrication of Various Ionic Sensors: The temperature sensors in Figure 2b–i were fabricated by printing silver electrodes (100 μm) on both sides of the viscous ionic gels (Length: 1.0 cm; Width: 1.0 cm; Height: 0.3 cm). The pressure-insensitive temperature sensors in Figure 2j,k were fabricated by printing silver electrodes (40 μm) on both sides of the viscous ionic gels (Length: 1.0 cm; Width: 1.0 cm; Height: 0.3 cm). The pressure sensors in Figure 3b–j were assembled by printing silver electrodes (100 μm) on both sides of the viscous ionic gels (Length: 1.0 cm; Width: 1.0 cm; Height: 0.3 cm). The temperature-pressure decoupled ionic sensors in Figure 4 were assembled by prepare the pressure-insensitive temperature sensor (Length: 0.4 cm; Width: 0.4 cm; Height: 0.04 cm) and pressure sensor (Length: 0.4 cm; Width: 0.4 cm; Height: 0.3 cm) on each side of the PET substrate. The test methods for these devices have been given in the section 2, 3 and 4 of the main text and the characterizations. Also, the fabrication of the sensor array was also given in the main text. Regarding the sensors integrated to the robotic arm, three different ionic sensors were assembled onto the index, middle, and ring fingers of the robotic arm. Each sensor was independently connected to the microcontroller that controlled the robot arm. When placing objects with different temperatures inside the robot's arm, the robot would make appropriate grasping or releasing movements due to the sensing of the temperature sensing layer.

Supporting Information

Supporting Information is available from the Wiley Online Library or from the author.

Acknowledgements

**ADVANCED
SCIENCE NEWS**

www.advancedsciencenews.com

**NANO · MICRO
small**

www.small-journal.com

Conflict of Interest

The authors declare no conflict of interest.

Data Availability Statement

The data that support the findings of this study are available from the corresponding author upon reasonable request.

Keywords

[1] S. H. Kim, K. Hong, W. Xie, K. H. Lee, S. Zhang, T. P. Lodge, C. D. Frisbie, *Adv. Mater.* **2013**, *25*, 1822.

[2] Y. Cai, J. Shen, Z. Dai, X. Zang, Q. Dong, G. Guan, L. J. Li, W. Huang, X. Dong, *Adv. Mater.* **2017**, *29*, 1606411.

[3] C. Wan, G. Chen, Y. Fu, M. Wang, N. Matsuhisa, S. Pan, L. Pan, H. Yang, Q. Wan, L. Zhu, *Adv. Mater.* **2018**, *30*, 1801291.

[4] Y. Liu, R. Bao, J. Tao, J. Li, M. Dong, C. Pan, *Sci. Bull.* **2020**, *65*, 70.

[5] C. Pan, L. Dong, G. Zhu, S. Niu, R. Yu, Q. Yang, Y. Liu, Z. L. Wang, *Nat. Photonics* **2013**, *7*, 752.

[6] Q. Shao, Z. Niu, M. Hirtz, L. Jiang, Y. Liu, Z. Wang, X. Chen, *Small* **2014**, *10*, 1466.

[7] Y. Cao, T. Li, Y. Gu, H. Luo, S. Wang, T. Zhang, *Small* **2018**, *14*, 1703902.

[8] G. Li, S. Liu, L. Wang, R. Zhu, *Sci. Rob.* **2020**, *5*, eabc8134.

[9] G. Loke, T. Khudiyev, B. Wang, S. Fu, S. Payra, Y. Shaoul, J. Fung, I. Chatziveroglou, P.-W. Chou, I. Chinn, *Nat. Commun.* **2021**, *12*, 3317.

[10] L. Yang, C. Liu, W. Yuan, C. Meng, A. Dutta, X. Chen, L. Guo, G. Niu, H. Cheng, *Nano Energy* **2022**, *103*, 107807.

[11] J. Fang, L. Zhang, J. Li, L. Lu, C. Ma, S. Cheng, Z. Li, Q. Xiong, H. You, *Nat. Commun.* **2018**, *9*, 521.

[12] R. Guo, X. Sun, S. Yao, M. Duan, H. Wang, J. Liu, Z. Deng, *Adv. Mater. Technol.* **2019**, *4*, 1900183.

[13] S. Zhang, J. Zhu, Y. Zhang, Z. Chen, C. Song, J. Li, N. Yi, D. Qiu, K. Guo, C. Zhang, *Nano Energy* **2022**, *96*, 107069.

[14] S. Omata, Y. Terunuma, *Sens. Actuators, A* **1992**, *35*, 9.

[15] H. Dong, L. Jiang, W. Hu, *Phys. Chem. Chem. Phys.* **2012**, *14*, 14165.

[16] T. Wang, A. Ramnarayanan, H. Cheng, *Sensors* **2017**, *18*, 5.

[17] Z. Liang, J. Cheng, Q. Zhao, X. Zhao, Z. Han, Y. Chen, Y. Ma, X. Feng, *Adv. Mater. Technol.* **2019**, *4*, 1900317.

[18] J. C. Yang, J. Mun, S. Y. Kwon, S. Park, Z. Bao, S. Park, *Adv. Mater.* **2019**, *31*, 1970337.

[19] L. Gu, S. Poddar, Y. Lin, Z. Long, D. Zhang, Q. Zhang, L. Shu, X. Qiu, M. Kam, A. Javey, *Nature* **2020**, *581*, 278.

[20] D. Wang, S. Zhao, R. Yin, L. Li, Z. Lou, G. Shen, *npj Flexible Electron.* **2021**, *5*, 13.

[21] X. Wang, Y. Liu, H. Cheng, X. Ouyang, *Adv. Funct. Mater.* **2022**, *32*, 2200260.

[22] F. Zhang, Y. Zang, D. Huang, C.-a. Di, D. Zhu, *Nat. Commun.* **2015**, *6*, 8356.

[23] H. Jia, X. Tao, Y. Wang, *Adv. Electron. Mater.* **2016**, *2*, 1600136.

[24] S. Lee, A. Reuveny, J. Reeder, S. Lee, H. Jin, Q. Liu, T. Yokota, T. Sekitani, T. Isoyama, Y. Abe, *Nat. Nanotechnol.* **2016**, *11*, 472.

[25] C. Wang, K. Xia, M. Zhang, M. Jian, Y. Zhang, *ACS Appl. Mater. Interfaces* **2017**, *9*, 39484.

[26] S. Han, J. Kim, S. M. Won, Y. Ma, D. Kang, Z. Xie, K.-T. Lee, H. U. Chung, A. Banks, S. Min, *Sci. Transl. Med.* **2018**, *10*, eaan4950.

[27] Q. Hua, J. Sun, H. Liu, R. Bao, R. Yu, J. Zhai, C. Pan, Z. L. Wang, *Nat. Commun.* **2018**, *9*, 244.

[28] S. Gong, L. W. Yap, B. Zhu, Q. Zhai, Y. Liu, Q. Lyu, K. Wang, M. Yang, Y. Ling, D. T. Lai, *Adv. Mater.* **2019**, *31*, 1903789.

[29] P. Li, Y. Zhang, Z. Zheng, *Adv. Mater.* **2019**, *31*, 1902987.

[30] C. Pan, J. Zhai, Z. L. Wang, *Chem. Rev.* **2019**, *119*, 9303.

[31] J. Shin, Y. Yan, W. Bai, Y. Xue, P. Gamble, L. Tian, I. Kandela, C. R. Haney, W. Spees, Y. Lee, *Nat. Biomed. Eng.* **2019**, *3*, 37.

[32] W. Zhang, L. Zhang, Y. Liao, H. Cheng, *Int. J. Extreme Manuf.* **2021**, *3*, 042001.

[33] F.-L. Gao, P. Min, X.-Z. Gao, C. Li, T. Zhang, Z.-Z. Yu, X. Li, *J. Mater. Chem. A* **2022**, *10*, 18256.

[34] R. Yang, W. Zhang, N. Tiwari, H. Yan, T. Li, H. Cheng, *Adv. Sci.* **2022**, *9*, 2202470.

[35] P. Zhu, Y. Wang, Y. Wang, H. Mao, Q. Zhang, Y. Deng, *Adv. Energy Mater.* **2020**, *10*, 2001945.

[36] G. Y. Bae, J. T. Han, G. Lee, S. Lee, S. W. Kim, S. Park, J. Kwon, S. Jung, K. Cho, *Adv. Mater.* **2018**, *30*, 1803388.

[37] X. Wu, J. Zhu, J. W. Evans, C. Lu, A. C. Arias, *Adv. Funct. Mater.* **2021**, *31*, 2010824.

[38] Y. Ding, J. Zhang, X. Zhang, Y. Zhou, S. Wang, H. Liu, L. Jiang, *Adv. Mater. Interfaces* **2015**, *2*, 1500177.

[39] H. Jia, Y. He, X. Zhang, W. Du, Y. Wang, *Adv. Electron. Mater.* **2015**, *1*, 1500029.

[40] Y. Liu, Y. Hu, J. Zhao, G. Wu, X. Tao, W. Chen, *Small* **2016**, *12*, 5074.

[41] S. Han, J. Zhao, D. Wang, C. Lu, W. Chen, *J. Mater. Chem. B* **2017**, *5*, 7126.

[42] J. Lee, M. O. F. Emon, M. Vatani, J.-W. Choi, *Smart Mater. Struct.* **2017**, *26*, 035043.

[43] C. X. Hu, Q. Xiao, Y. Y. Ren, M. Zhao, G. H. Dun, H. R. Wu, X. Y. Li, Q. Q. Yang, B. Sun, Y. Peng, *Adv. Funct. Mater.* **2018**, *28*, 1805311.

[44] Z. Lei, P. Wu, *Nat. Commun.* **2018**, *9*, 1134.

[45] Z. Wang, Y. Si, C. Zhao, D. Yu, W. Wang, G. Sun, *ACS Appl. Mater. Interfaces* **2019**, *11*, 27200.

[46] X. Yang, Y. Wang, H. Sun, X. Qing, *Sens. Actuators, A* **2019**, *285*, 67.

[47] Y. Cai, J. Shen, C.-W. Yang, Y. Wan, H.-L. Tang, A. A. Aljarb, C. Chen, J.-H. Fu, X. Wei, K.-W. Huang, *Sci. Adv.* **2020**, *6*, eabb5367.

[48] N. Gao, X. Wu, Y. He, Q. Ma, Y. Wang, *Adv. Electron. Mater.* **2020**, *6*, 1901388.

[49] S.-Y. Zhang, Q. Zhuang, M. Zhang, H. Wang, Z. Gao, J.-K. Sun, J. Yuan, *Chem. Soc. Rev.* **2020**, *49*, 1726.

[50] Y. Ren, Z. Liu, G. Jin, M. Yang, Y. Shao, W. Li, Y. Wu, L. Liu, F. Yan, *Adv. Mater.* **2021**, *33*, 2008486.

[51] X. Fu, Z. Zhuang, Y. Zhao, B. Liu, Y. Liao, Z. Yu, P. Yang, K. Liu, *ACS Appl. Mater. Interfaces* **2022**, *14*, 44792.

[52] C. Liang, C.-Y. Yuan, R. J. Warmack, C. E. Barnes, S. Dai, *Anal. Chem.* **2002**, *74*, 2172.

[53] Y.-N. Cheung, Y. Zhu, C.-H. Cheng, C. Chao, W. W.-F. Leung, *Sens. Actuators, A* **2008**, *147*, 401.

[54] C.-Y. Wu, W.-H. Liao, Y.-C. Tung, *Lab Chip* **2011**, *11*, 1740.

[55] B. Nie, R. Li, J. D. Brandt, T. Pan, *Lab Chip* **2014**, *14*, 4344.

[56] H. Ota, K. Chen, Y. Lin, D. Kiriya, H. Shiraki, Z. Yu, T.-J. Ha, A. Javey, *Nat. Commun.* **2014**, *5*, 5032.

[57] C. Yang, Z. Suo, *Nat. Rev. Mater.* **2018**, *3*, 125.

[58] N. Gao, Y. He, X. Tao, X.-Q. Xu, X. Wu, Y. Wang, *Nat. Commun.* **2019**, *10*, 547.

[59] N. Bai, L. Wang, Q. Wang, J. Deng, Y. Wang, P. Lu, J. Huang, G. Li, Y. Zhang, J. Yang, *Nat. Commun.* **2020**, *11*, 209.

[60] H. J. Kim, B. Chen, Z. Suo, R. C. Hayward, *Science* **2020**, *367*, 773.

[61] T. Li, Y. Wang, S. Li, X. Liu, J. Sun, *Adv. Mater.* **2020**, *32*, 2002706.

[62] H. Liu, X. Wang, Y. Cao, Y. Yang, Y. Yang, Y. Gao, Z. Ma, J. Wang, W. Wang, D. Wu, *ACS Appl. Mater. Interfaces* **2020**, *12*, 25334.

[63] Y. N. Ye, K. Cui, W. Hong, X. Li, C. Yu, D. Hourdet, T. Nakajima, T. Kurokawa, J. P. Gong, *Proc. Natl. Acad. Sci. U. S. A.* **2021**, *118*, e2014694118.

[64] Y. A. Nikolaev, V. V. Feketa, E. O. Anderson, E. R. Schneider, E. O. Gracheva, S. N. Bagriantsev, *Sci. Adv.* **2020**, *6*, eabe6393.

[65] S. Feng, Q. Li, S. Wang, B. Wang, Y. Hou, T. Zhang, *ACS Appl. Mater. Interfaces* **2019**, *11*, 21049.

[66] Z. Wang, L. Zhang, J. Liu, C. Li, *Nanoscale* **2019**, *11*, 14242.

[67] J. Sun, G. Lu, J. Zhou, Y. Yuan, X. Zhu, J. Nie, *ACS Appl. Mater. Interfaces* **2020**, *12*, 14272.

[68] N. Jiang, H. Li, D. Hu, Y. Xu, Y. Hu, Y. Zhu, X. Han, G. Zhao, J. Chen, X. Chang, *Compos. Commun.* **2021**, *27*, 100845.

[69] S.-L. Zuo, P. Chen, C.-F. Pan, *Rare Met.* **2020**, *39*, 1113.

[70] V. Amoli, J. S. Kim, S. Y. Kim, J. Koo, Y. S. Chung, H. Choi, D. H. Kim, *Adv. Funct. Mater.* **2020**, *30*, 1904532.

[71] Z. Chen, Q. Gui, Y. Wang, *Green Chem. Eng.* **2021**, *2*, 346.

[72] Z. Chen, Y. He, X. Tao, Y. Ma, J. Jia, Y. Wang, *J. Phys. Chem. Lett.* **2022**, *13*, 10076.

[73] Z. Chen, Y. Wang, *Sens. Diagn.* **2022**, *1*, 598.

[74] Z. Chen, Y. Wang, *Ind. Chem. Mater.* **2023**, *1*, 224.

[75] N. Gao, Q. Ma, Y. He, Y. Wang, *Chem. J. Chin. Univ.* **2020**, *41*, 901.

[76] Q. Gui, Y. He, Y. Wang, *Adv. Electron. Mater.* **2021**, *7*, 2000780.

[77] I. You, D. G. Mackanic, N. Matsuhisa, J. Kang, J. Kwon, L. Beker, J. Mun, W. Suh, T. Y. Kim, J. B.-H. Tok, *Science* **2020**, *370*, 961.

[78] S. Hu, Z. Zhang, Y. Zhou, J. Song, H. Fan, B. Han, *Green Chem.* **2009**, *11*, 873.

[79] S. Zhang, J. Sun, X. Zhang, J. Xin, Q. Miao, J. Wang, *Chem. Soc. Rev.* **2014**, *43*, 7838.

[80] X. Gao, B. Yu, Z. Yang, Y. Zhao, H. Zhang, L. Hao, B. Han, Z. Liu, *ACS Catal.* **2015**, *5*, 6648.

[81] Z. Zhang, X. Zhang, Y. Nie, H. Wang, S. Zheng, S. Zhang, *Sci. China: Chem.* **2017**, *60*, 934.

[82] T. Ge, J.-D. He, L. Xu, Y.-H. Xiong, L. Wang, X.-W. Zhou, Y.-P. Tian, Z. Zhao, *Rare Met.* **2023**, *42*, 1118.